electronics

MDPI

Article

High Efficiency Converters Based on Modular Partial Power Processing for Fully Electric Maritime Applications

Jon Anzola *, Erik Garayalde, June Urkizu, Argiñe Alacano and Ramon Lopez-Erauskin

Faculty of Engineering, Mondragon Unibertsitatea, 20120 Hernani, Spain; egarayalde@mondragon.edu (E.G.); jurkizu@mondragon.edu (J.U.); aalacano@mondragon.edu (A.A.); rlopez@mondragon.edu (R.L.-E.)
* Correspondence: janzola@mondragon.edu

Abstract: This paper proposes an approach for analyzing the benefits that partial-power-processing-based converters can bring to fully electric maritime applications. With the aim of making the system modular and scalable to different powers/energies, series-connected partial power converters are proposed. Serializing these converters entails significant overvoltage issues, and this paper tackles them for one series-connected module failure case. A reliability analysis has been carried out considering that the components of the battery system follow an independent and identical distribution in terms of failure probability. Furthermore, a redundancy factor has been added to allow a certain failure rate in what is known as a fault-tolerant system. Finally, to demonstrate the high efficiency of partial power converters, a 3 kW prototype is tested at different working points that model the charging process of a battery. The experimental results show a peak efficiency of 99.36%.

Keywords: electric vessel; energy storage system (ESS); hybrid; modular converter; DC–DC power converter; partial power processing (PPP); partial power converter (PPC); dual active bridge (DAB)

Citation: Anzola, J.; Garayalde, E.; Urkizu, J.; Alacano, A.; Lopez-Erauskin, R. High Efficiency Converters Based on Modular Partial Power Processing for Fully Electric Maritime Applications. *Electronics* **2023**, *12*, 2778. https://doi.org/10.3390/electronics12132778

Academic Editor: Fabio Corti

Received: 16 May 2023
Revised: 20 June 2023
Accepted: 21 June 2023
Published: 23 June 2023

1. Introduction

Waterborne transport contributed to around 14% of all greenhouse gas (GHG) emissions from transport in the European Union in 2018, representing about 2.8% of total human-made emissions that year. In total, European ships generated 140 million tons of CO_2 emissions, approximately 18% of all CO_2 emissions generated by maritime transport worldwide [1,2]. If carbon intensive modes of transport continue to grow as expected [3], maritime transport could face a 50–250% GHG emission increase by 2050. In line with the Paris Agreement goals, in 2018, the International Maritime Organization (IMO) developed a strategy to reduce the shipping industry's GHG emissions by at least 50% by 2050 compared with their level in 2008 [4,5].

A promising solution to reach this target is the electrification of the maritime sector. Indeed, the increasing amount of hybrid and full-electric vessels reflects the interest of ship operators, shipbuilders, fleet service providers, and other actors involved in maritime transportation to electrically retrofit fuel-based fleets, or even to acquire newbuild electrical vessels [6,7]. However, the current technology is not yet mature, and the batteries used in this sector are considerably more expensive than automotive ones [8]. Battery propulsion is not so evident, as batteries have technical limitations such as energy density, power density, and lifetime. The choice of storage technology therefore influences the operational performance of ships, such as speed and range. In addition, batteries have other shortcomings to take into account when using them in this application, such as their cost, cycle life, safety, and the need for fast-recharging infrastructure on shore [7]. Usually, on-board, electrical energy storage systems for maritime applications are characterized by including only a single type of battery cell technology. Hence, the monotype battery is used for different energy demand missions (maintaining cruising speed, maneuvering, fast charging, etc.), i.e., without differentiating between high-energy (HE) and high-power (HP) operations.

This results in battery systems with excessive energy or power capacity, increasing the cost, weight, and volume of the solution and making it inflexible [9]. In the literature, hybrid energy storage systems have been proposed for many different operating strategies, such as filtering, rule-based limitations of the operating window of the high-energy battery, or optimized load splitting for predefined load profiles [10–14]. To seek the best aboard energy sources for waterborne transport, many electrical energy storage combinations able to suit ship applications are being examined in terms of price, autonomy, and lifetime [15,16]. Nevertheless, to date, hybridization is not a common practice in waterborne transport electrical systems. The development of hybrid energy storage systems (HESS) makes it possible to take full advantage of the characteristics that each technology possesses, depending on the HE or HP demand of the load. This way, the storage system gets optimized, avoiding the need for oversized batteries. Hence, determining the optimal sizing of the HESS is crucial for achieving those benefits.

Just as important as having the possibility to use different type of batteries for both HE and HP operations is the implementation of high efficiency converters [17–19] that can adapt the energy provided by the batteries to ensure a stable output voltage of the HESS. Power electronic converters play a key role in the interface between the energy storage systems (ESS) and the distribution network of the ship. Usually, the battery-based ESS is connected to the distribution system through a single bidirectional full power converter, although recent studies propose distributed concepts based on series and/or parallel connection of modules composed of a single cell and a converter [20]. Regarding the types of DC/DC converters used in maritime applications, the Dual Active Bridge (DAB), the three-level Neutral Point Clamped (3L-NPC), or the isolated Modular Multilevel Converter (iMMC) are possible [20]. It should be noted that all of them operate by processing all input power, i.e., they are used as full power converters. This leads to higher voltage-current rated components, which are related to a higher cost and bigger volume, and, in addition, by using a single converter, the reliability of the system is compromised in case of converter failure. On the other hand, when working at high power, power electronic devices are usually heavy and take up a lot of space. As the DC/DC converter is a power conversion device, one of the most important characteristics to pay attention to is its energy efficiency. Therefore, smaller size, lighter and higher efficiency power converters are required in maritime applications [21].

The recent literature around electric vehicle fast charging applications presents advanced architectures based on partial power processing (PPP) [22,23]. These types of strategies aim to reduce the power to be processed by the power converter, achieving more efficient and downsized solutions [23–25]. Indeed, PPP-based converters have been proposed for a broad variety of unidirectional power flow applications. These converters are usually placed in series with an energy storage bank, and they are suitable for DC–DC applications where the voltage difference between the input and output terminals is not very high. According to [26], PPP strategies for DC–DC applications are classified into three different groups: differential power converters, partial power converters (PPC), and mixed strategies. This work is focused on the implementation of PPCs, which control the total power flow between two elements by only processing a portion of the total power [27–29]. The interest of this article relies on the analysis of the modularity of PPCs to meet high power and/or energy demands. The literature shows that the parallel connection of PPCs does not present mayor challenges compared to the full power converters [30,31]. However, there is a lack of research on series-connected PPCs. The performance of PPCs is highly dependent on the voltage gain of the application. Therefore, this article presents a sizing method for parallel- and series-connected modular PPCs.

For all the above reasons, developing modular HESS and high efficiency converters will be key in the electrification of the maritime sector and, thus, to meet GHG emissions reduction goals. Therefore, this paper presents a HESS based on modular PPC (see Figure 1) suitable for HE and HP operations in a fully electric vessel that enhances the flexibility and scalability of the system. The main contribution of this work is the use of PPC in these

applications and, in particular, their series connection. Each DC–DC converter is in charge of controlling the power flow of a single ESS. The group formed by an ESS and a DC–DC converter will hereinafter be referred as an ESS module. Depending on the cell technology used, the ESS modules can be HE or HP modules. The ESS modules are connected in series, forming a string of several HE or HP modules to reach the desired string voltage and making the system scalable. Finally, different strings in parallel form the HESS.

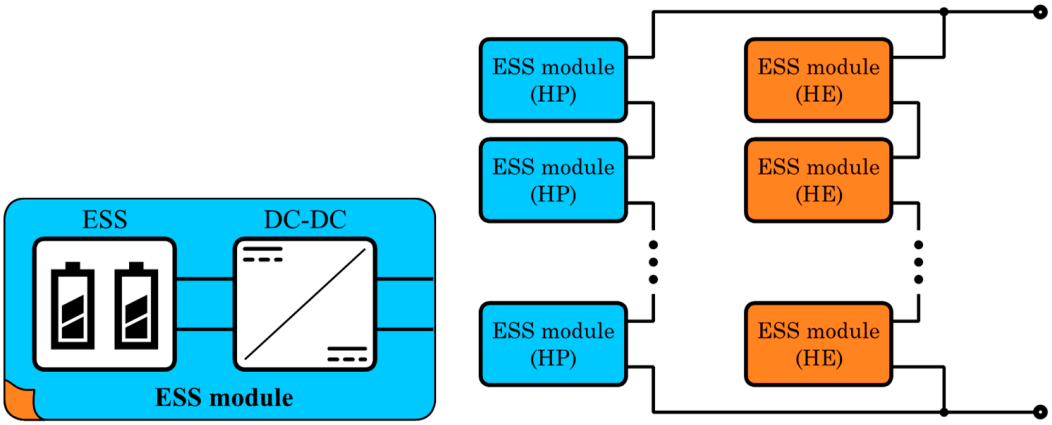

Figure 1. The HESS architecture comprises strings of series-connected HP modules, connected in parallel with strings of series-connected HE modules.

This paper is divided in the following sections: in Section 2, the HESS sizing and hybridization analysis is conducted for a specific use case, whereas Section 3 describes the design of the modular PPC, taking into account the reliability analysis of the battery system. Finally, Section 4 presents the modeling of the modular PPC solution and the simulations results, and in Section 5, a 3 kW PPC prototype is tested at different working points that model the charging process of a battery.

2. Hybrid Energy Storage System Design

2.1. Electric Vessel Power Profile

According to [32–34], the electrification of ships mainly takes place on ferries that usually follow the same route. A real power profile of an electric urban ferry (Figure 2), has been used as the starting point for the dimensioning of the HESS. The power profile consists of two cycles: During half of the year (183 days), it makes eight short trips per day with high-power demand. The rest of the year (182 days), the short trip is repeated seven times followed by a larger one, consuming more energy.

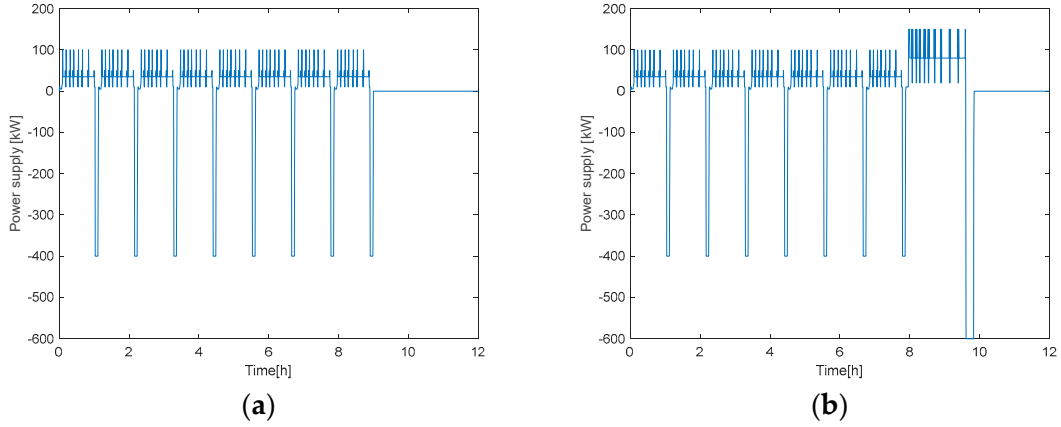

Figure 2. Electric urban ferry load profile. (**a**) First cycle of 8 short trips. (**b**) Second cycle of 7 short trips and a larger one. Courtesy: Damen shipyards group.

2.2. HESS Cells Selection

The use of lithium-ion batteries for electric mobility and, more specifically, for waterborne transport is extensive, as shown in [35–38]. The variety of lithium-ion battery cells in the market is large depending on the material and properties of the electrolyte and electrodes. Those materials and properties provide the cells with different characteristics. Certain cells are notable for their high specific energy, such as, nickel–manganese–cobalt oxide (NMC) and nickel–cobalt–aluminum oxide (NCA), making them suitable for applications with higher energy demands. Antagonist cell technologies exhibit higher power densities, so they are used in applications where the power requirement is high, e.g., lithium–iron–phosphate (LFP) and lithium–titanate oxide (LTO), among others [39–41].

In battery cell technology, the increment of the energy density occurs at the cost of decreasing the power capability of the cell. A common practice is to oversize the battery system to cover the energy and power required by the application Figure 3.

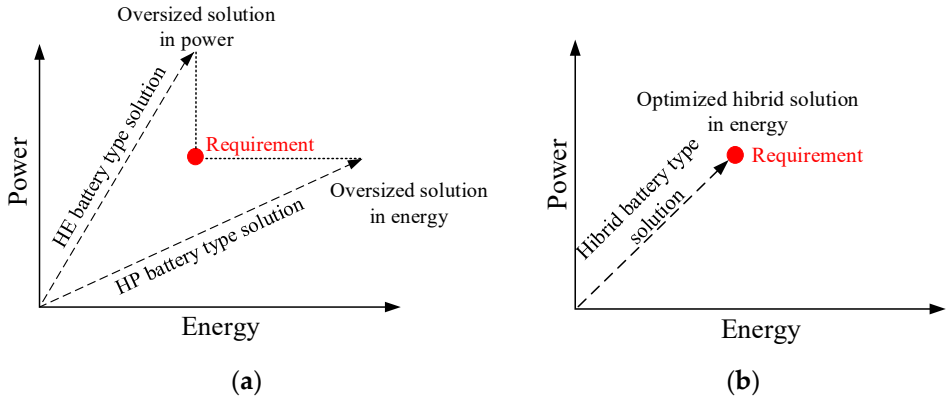

Figure 3. Battery solutions for different energy-demand applications. (**a**) The battery is oversized to fulfill energy and power requirements in case of using a unique battery type (HP or HE). (**b**) The dimensioning can be optimized using a hybrid battery. Own figure based on [42].

Alternatively, hybridization allows the system to obtain high-power and high-energy capabilities while using the best properties of two battery technologies. Indeed, hybridization brings significant advantages concerning weight, volume, and investment [42]. To design the HESS, LTO technology is selected as high-power (HP) technology because of its high power density. On the other hand, NMC cells are selected as high-energy (HE) cells because of their good energy density [14].

2.3. Monotype vs. Hybrid Battery Sizing

Considering the proposed battery technologies and the power profile of the urban ferry, the evaluation of the storage system has been carried out taking into account the specifications shown in Table 1:

Table 1. Storage system specification.

Battery Cells	**Samsung SDI 94 Ah NMC 0.109 €/Wh Toshiba SCiB 23 Ah LTO 0.43 €/Wh**
Typically required minimum lifetime in maritime applications	10 years
Maximum power peak of the profile	150 kW
Minimum stored energy of the profile	136 kWh
Maximum DC bus voltage (below limits of Low Voltage Directive)	1000 V
State of Charge range of the batteries	Between 90% and 10% (safety margin)

The sizing of the urban ferry ESS by considering monotype HE or HP system is gathered in Table 2. In the case of choosing a NMC ESS, more power and energy are

installed due to its higher degradation, but the battery pack is cheaper due to the lower price of the NMC cells.

Table 2. Dimensioning of the battery system in case of having HE or HP cells.

	Monotype HE	**Monotype HP**
Battery cells	Samsung SDI 94Ah NMC	Toshiba SCiB 23Ah LTO
Cells layout	224S10P	352S12P
Peak power	1393.1 kW	1049.2 kW
Energy	774.9 kWh	223.4 kWh
Cost	82,910 €	96,083 €

On the other hand, when working with two technologies (NMC and LTO), a power split control is necessary to decide the amount of power that will be provided by each technology. For the sake of simplicity, this paper proposes a power split that limits the maximum power supplied by the HE battery. This way, HE batteries operate under stable working cycle conditions and HP batteries will cover variable load demands, such as speed variations or port maneuvers.

In order to reduce the cost of the HESS, different HE power limits have been defined to find the case with the lowest possible cost, i.e., the optimal one. Figures 4 and 5 show, respectively, the flowchart of the HESS's cost for different HE power limits and its results Figure 5.

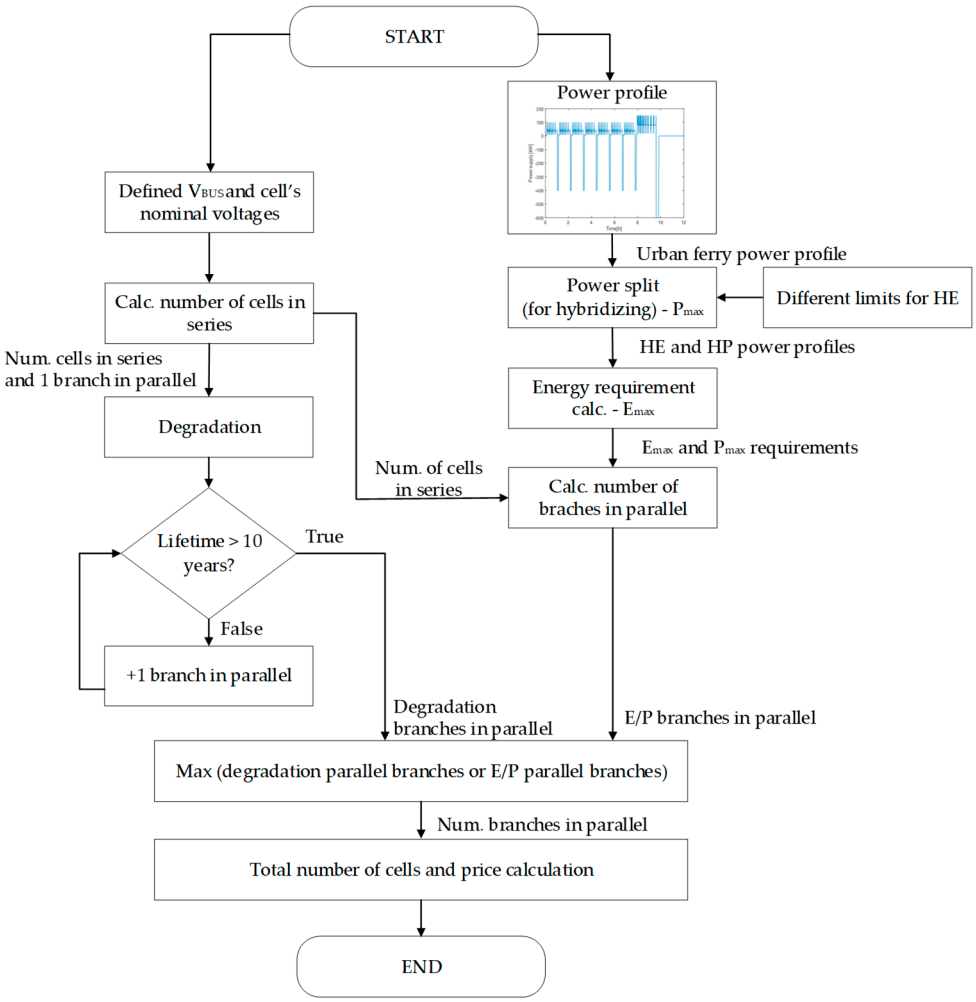

Figure 4. HESS sizing and cost calculation flowchart.

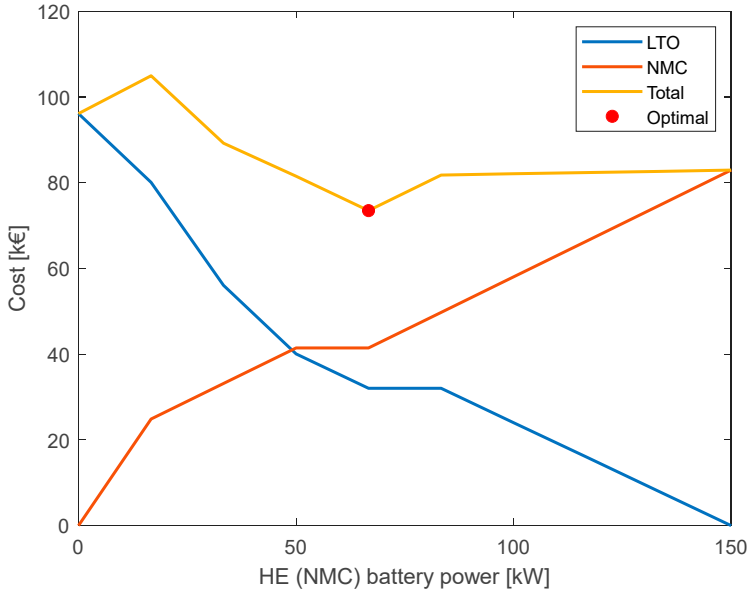

Figure 5. Cost of the HESS depending on the HE power limit (NMC power limit). The leftmost cost value corresponds to a full HP battery. The rightmost cost value corresponds to a full HE battery. The mid-point cost value corresponds to the hybridization case where the HE and HP are sized to give the same total power.

By limiting the HE battery power to the optimal operation point, i.e., 66.66 kW, the cheapest battery system is achieved. The sizing of the battery for this case can be seen in Table 3.

Table 3. Dimensioning of the battery system in case of having both HE and HP cells, implementing the cheapest HESS.

	Hybrid Battery		**Total**
	HE	**HP**	**HE + HP**
Cells layout	224S5P	352S4P	
Power	696.5 kW	349.7 kW	1046.2 kW
Energy	387.4 kWh	74.5 kWh	461.9 kWh
Cost	32,028 €	41,455 €	73,483 €

Although the HE battery is initially limited to 66.6 kW as the most optimal point (Figure 5), it is necessary to oversize it to meet State of Charge (SoC) and lifetime requirements. Considering them, the final size of the HE battery is 696.5 kW and 387.4 kWh, although the real operating point will be limited to 66.6 kW. The same occurs with the HP battery. Although it is initially sized for 84 kW as the most optimal point, it is oversized to 349.7 kW to meet the requirements.

Even if the battery is oversized, comparing the results of Tables 2 and 3, the power sizing in the case of hybridization is the most optimal. Furthermore, if the prices of the battery packs are compared, the savings for installing a hybrid battery would be 9427 € (11.4 %) in the case of replacing a pure NMC battery and 22,600 € (23.5 %) to replace a pure LTO battery.

The power split of the electric urban ferry load is shown in Figure 6, where the power of the HE power is limited to 66.66 kW.

It has been shown that hybridization can be cost-effective, but the price of each technology has a strong influence on it. If LTO battery prices decrease in the future, hybridization might not be profitable.

Once the battery pack has been sized for an urban ferry application, it is necessary to pay attention to the efficiency of the conversion stage, i.e., the converter.

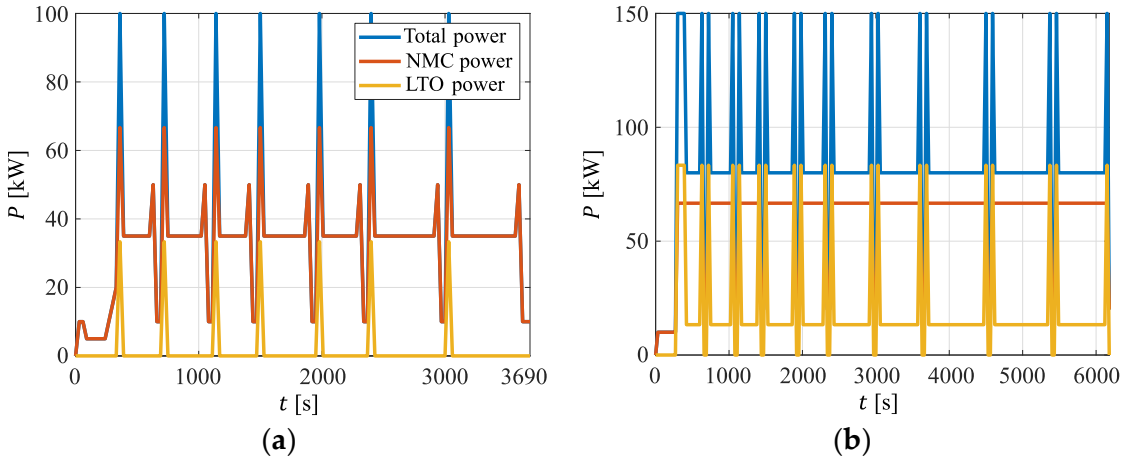

Figure 6. Urban ferry's power profile. (**a**) Short trip. (**b**) Long trip.

3. Modular PPC Design

Within the family of PPC, there are two main architectures: Input-Parallel–Output-Series (IPOS, Figure 7a) and Input-Series–Output-Parallel (ISOP, Figure 7b). Depending on the operating conditions, each architecture achieves a different reduction of the power processed by the converter. This can be compared by calculating the partial power ratio (K_{pr}), which consists of the ratio of the converter power (P_{conv}) to the system power (P_{source}). Applying Kirchhoff's laws, K_{pr} curves of both architectures are obtained as a function of the static voltage gain (G_V) and are defined in (1)–(4) [43].

$$K_{pr} = \frac{P_{conv}}{P_{source}} \tag{1}$$

$$K_{pr_{IPOS}} = \eta_{system} - \frac{\eta_{system}}{G_V} \tag{2}$$

$$K_{pr_{ISOP}} = \eta_{system} - G_V \tag{3}$$

$$G_V = \frac{V_{load}}{V_{source}} \tag{4}$$

where $K_{pr_{IPOS}}$ and $K_{pr_{ISOP}}$ are the processed power ratios of the IPOS and ISOP architectures. η_{system} is the efficiency of the system, which is given in (5).

$$\eta_{system} = \frac{V_{load} \cdot I_{load}}{V_{source} \cdot I_{source}} \tag{5}$$

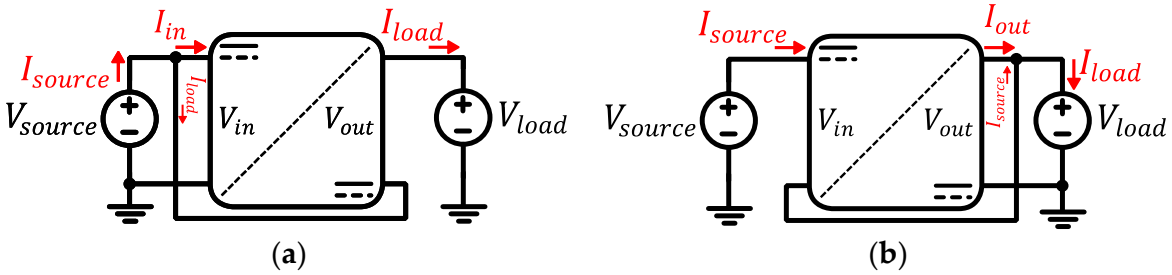

Figure 7. PPC architectures. (**a**) IPOS. (**b**) ISOP.

Equations (2) and (3) are plotted in Figure 8, where η_{system} is considered ideal.

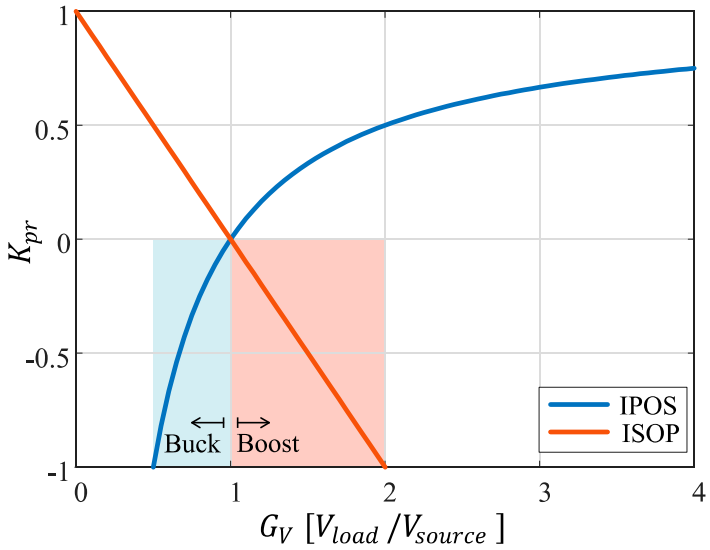

Figure 8. K_{pr} curves of IPOS and ISOP architectures.

Analyzing Figure 8, several conclusions can be drawn. First, it is observed that as G_V approaches 1, the value of K_{pr} decreases. That is, the smaller the voltage gain, the less power the converter will process. This is the same for both architectures.

Secondly, if the application requires only voltage boost ($G_V > 1$), the architecture that obtains lower K_{pr} values is IPOS. In fact, its K_{pr} curve never exceeds the value of 1 when working in boost mode, meaning that the converter will process only a part of the total power transferred to the load. On the contrary, the ISOP architecture obtains K_{pr} values less than -1 when G_V is greater than 2. Beyond that value, the converter does not operate in the partial power range, thus losing all advantages.

Thirdly, if the application requires only to reduce the voltage ($0 < G_V < 1$), the architecture that obtains lower K_{pr} values is the ISOP. As in the previous case, in buck mode, the ISOP architecture never exceeds the value of 1 for K_{pr}. However, the IPOS architecture does when G_V is less than 0.5.

Finally, if the application requires buck-boost functionality, the power converter will enter in the shaded blue (IPOS case) and red (ISOP case) areas from Figure 8. At these regions, the K_{pr} curve achieves negatives values, which means that the power flow inside the converter is reversed [44]. In the case of the IPOS, the polarization of V_{out} is inverted and the flow of I_{in} changes its direction to the opposite way. The same thing occurs with the ISOP for step-up applications. In this case, the polarity of V_{in} and the direction of I_{out} must be inverted.

To sum up, the IPOS architecture is the optimal solution for purely boost applications and the ISOP is optimal for purely buck applications. If the application consists of a buck-boost, the selection between the IPOS and the ISOP is not that evident and it requires a more complex comparison. Furthermore, the circuit inside the converter requires a higher number of components [44]. As presented in [44], in order to achieve buck-boost capabilities, both IPOS and ISOP architectures require the back-to-back connection between two semiconductors. These could be a diode and a MOSFET of double MOSFET.

Bearing in mind that the concerned converter is located between an ESS and a DC voltage, it is concluded that the most feasible solution in terms of number of cells is to work in boost mode when discharging the ESS. This means that in an IPOS architecture (Figure 7a), the ESS represents the source and the DC voltage represents the load. When charging the ESS, a reverse power flow will exist (buck mode) and the ISOP architecture will be imposed (Figure 7b). At this working point, the DC voltage will act as the source and the ESS will act as the load.

3.1. Modular PPC Dimensioning

The aim of the present article is to design a modular PPC that can be scalable in series and parallel for different applications and a flexible battery system. This subsection describes the design procedure to define the number of series-connected modules (n_s) and the number of series-connected cells per module (n_{cell_m}). Figure 9 shows a simplified electric diagram of a single string. As it can be observed, each module consists of four main voltages: battery cell voltage (V_{cell}), battery module voltage ($V_{bat} = n_{cell_m} \cdot V_{cell}$), converter output voltage (V_{out}), and module output voltage ($V_{mod} = V_{DC}/n_s$). V_{DC} is the DC bus voltage.

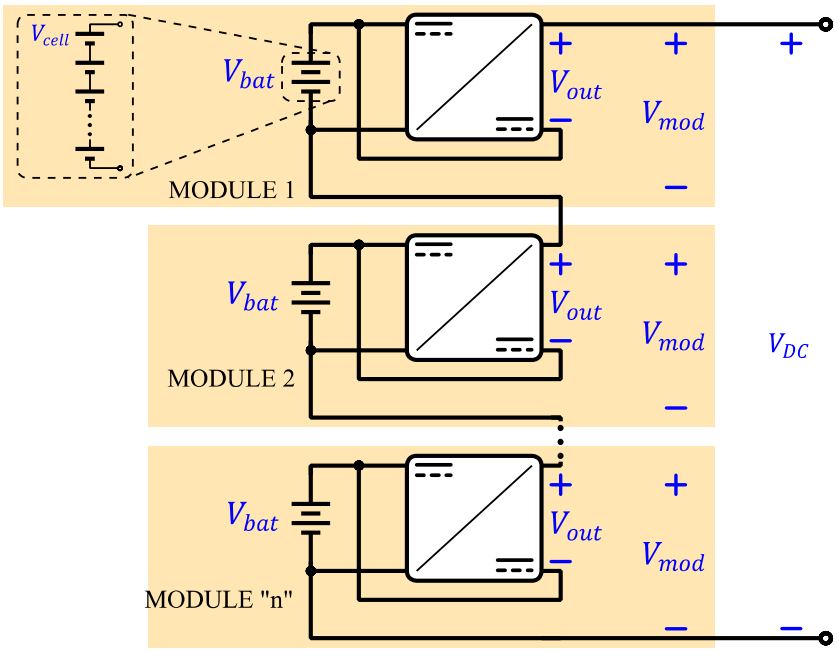

Figure 9. Modular series configuration of the PPC topology.

3.1.1. Preliminary Considerations

The K_{pr} curve of an IPOS architecture, such as the one shown in Figure 9, is defined as in (6). There, it can be observed that K_{pr} is directly dependent on G_V, which in this case is defined as the division between $V_{load} = V_{mod}$ and $V_{source} = V_{bat}$ (7).

$$K_{pr} = \frac{P_{conv}}{P_{mod}} = 1 - \frac{1}{G_V} \tag{6}$$

$$G_V = \frac{V_{mod}}{V_{bat}} = \frac{V_{DC}/n_s}{V_{bat}} \tag{7}$$

Focusing on (7), V_{mod} is considered as a constant parameter, since it is defined by V_{DC} and n_s. On the other hand, V_{bat} is considered as a variable parameter, since it depends on the SoC of the battery. In an ideal case, the lowest achievable G_V is given when the maximum value of the battery ($V_{bat_{max}}$) coincides with V_{mod}. In this case, G_V will obtain a value of 1 and the power processed by the converter would be 0. However, as the battery discharges, V_{bat} reduces until the battery is totally discharged ($V_{bat_{min}}$). This will be the most critical point of the converter in terms of processed power (8), (9).

$$G_V^* = \frac{V_{mod}}{V_{bat_{min}}} = \frac{V_{bat_{max}}}{V_{bat_{min}}} = \frac{n_{cell_m} \cdot V_{cell_{max}}}{n_{cell_m} \cdot V_{cell_{min}}} = \frac{V_{cell_{max}}}{V_{cell_{min}}} \tag{8}$$

$$K_{pr}^* = 1 - \frac{1}{G_V^*} \tag{9}$$

K^*_{pr} represents the minimum value that can be defined for the design value of K_{pr}. Due to the fact that n_{cell_m} needs to be an integer number, it is very rare to make coincide the values of $V_{bat_{max}}$ and V_{mod}. Therefore, K_{pr} (also known as $K_{pr_{MAX}}$) must be defined slightly higher than K^*_{pr} (10). Together with it, the maximum permitted $G_{V_{MAX}}$ can be obtained (11).

$$K_{pr_{MAX}} > K^*_{pr} \tag{10}$$

$$G_{V_{MAX}} = \frac{1}{1 - K_{pr_{MAX}}} \tag{11}$$

3.1.2. Number of Cells Per Module

It must be mentioned that n_s consists of a vector with integer values from 2 to 20. Thus, the first step consists of calculating the corresponding n_{cell_m} value for each n_s. This is obtained by applying Equations (12) and (13).

$$V_{bat_{min}} = \frac{V_{mod}}{G_{V_{MAX}}} = \frac{V_{DC}/n_s}{G_{V_{MAX}}} \tag{12}$$

$$n_{cell_m} = \left\lceil \frac{V_{bat_{min}}}{V_{cell_{min}}} \right\rceil \tag{13}$$

Due to the cell operation in (13), it is possible that the resulting $V_{bat_{max}}$ obtains a higher value than V_{mod}. This would suppose a voltage step-down working condition ($G_V < 1$), which implies a bipolar V_{out} and a more complex circuit. For this reason, it must be ensured that G_V gives a value greater than 1 for each n_s. In case the resulting G_V is lower than 1, that n_s is deleted.

3.1.3. Number of Modules

The total number of modules of the final solution will result from the product between the modules connected in series and the number of strings connected in parallel. The number of strings will be given by the total maximum power of the application and the power capability of the batteries. However, the definition of the number of modules in series is not that evident. Therefore, the present section aims to describe the steps followed to define the necessary number of modules in series.

The PPC architecture is focused on reducing the power processed by the converter and, thus, implementing lower rated components. Bearing this in mind, this analysis proposes to optimize the concerned reduction by considering that in case a single module fails, the rest of the modules must assume the resulting overload.

If one of the modules fails in Figure 9, the whole string stops working. In order to avoid this, it is suggested to design the converters for a possible one-module failure. This way, the concerned module would be short-circuited, and the rest of the modules would increment their power and voltage levels. Concerning this, the present analysis aims to select the value of n_s that minimizes the possible overload of the K_{pr} and the V_{out}.

With this purpose, two different cases are analyzed:K_{pr} and V_{out} for each value of n_s (nominal conditions) and for $n_s - 1$ (1 module fail). On the one hand, Figure 10a presents the obtained results for the K_{pr} parameter. As it can be observed, as the number of modules increases, the K_{pr} increment reduces. This means that the more modules are implemented, the less overload will exist in case one of them fails.

On the other hand, Figure 10b shows the obtained results for the V_{out} parameter. Similar to the K_{pr} analysis, as the value of n_s increases, a lower overvoltage is expected at the output of the converter in case one of the modules fails. Based on these results, it is decided to define n_s = 8. With this value, the expected overvoltage for both technologies (NMC and LTO) goes from 37 V to 55 V. This way, a 100 V rated switch with a lower on resistance can be implemented without taking any risk.

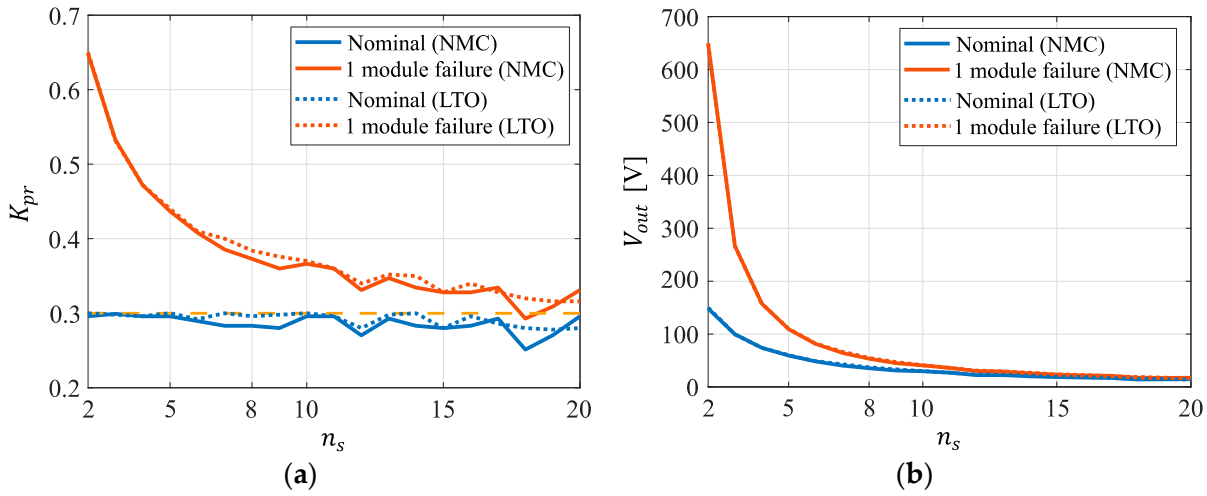

Figure 10. (**a**) K_{pr} increment for one module failure (**b**). V_{out} increment for one module failure.

Finally, bearing in mind that $n_s = 8$, the number of cells per module (n_{cell_m}) is calculated for each battery technology by using (12) and (13): $n_{cell_m} = 28$ (NMC) and $n_{cell_m} = 44$ (LTO). Then, the maximum voltage of the battery module is computed (14). The obtained $V_{bat_{max}}$ are used as input in the HESS sizing section.

$$V_{bat_{max}} = n_{cell_m} \cdot V_{cell_{max}} \quad (14)$$

To sum up, Figure 11 presents a flowchart of the previously discussed steps.

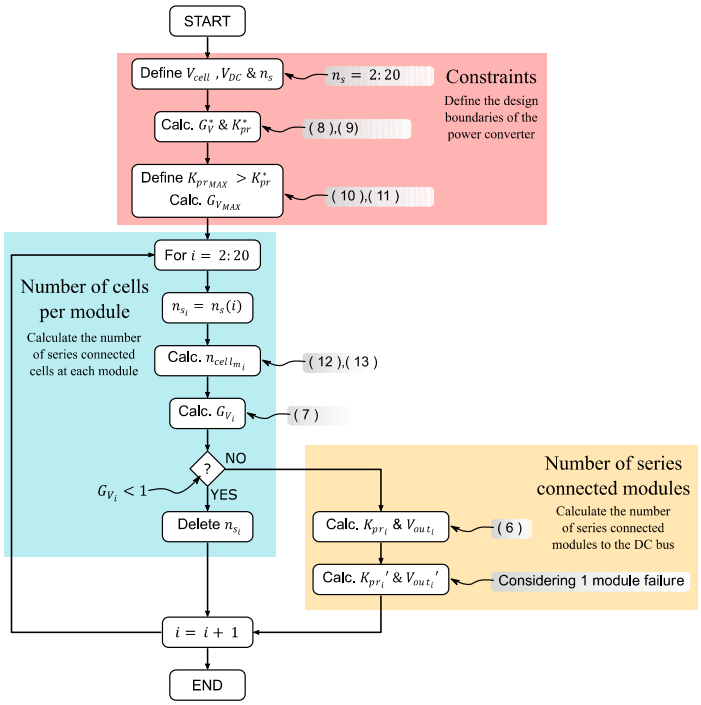

Figure 11. Block diagram of the number of cells (n_{cell_m}) and number of series-connected modules (n_s) selection process.

3.2. Reliability Analysis

To perform the reliability analysis of the system, the first step is to define the states of the system and the degree of redundancy that it will have. If we consider a system with redundancy, we will have a minimum of three possible states: completely working

(full performance), partially working (reduced performance) and completely failed (out of service)

The system will be sized with a certain number of cells in series and parallel to meet the power and energy requirements of the application. Besides that, series and parallel redundancy factors can be added allowing a certain failure rate in what is known as fault-tolerant system. Otherwise, if one element fails, the whole system could not continue operating.

Among the existing reliability calculation methods used for electronic devices, the empirical prediction method based on statistical curve fitting of historical failure data is chosen [45]. Applying the parts count prediction method employed by the MIL-HDBK-217, the failure rate of our module (λ_M) is estimated as follows in (15),

$$\lambda_M = \sum_{j=1}^{J} N_j(\lambda_g \pi_Q) \tag{15}$$

where λ_g is the generic failure rate for the jth generic part; π_Q is the corresponding quality factor; N_j is the quantity of the jth generic part; and J is the number of different generic part categories in the equipment.

The failure rates of the components that make up a module are shown in Table 4. The values of the components that make up the converter were obtained from the MIL-HDBK-217 database [46]. As for batteries, if lithium-ion battery cells are operated within manufacturer recommended limits, its failure rate is estimated to be 1 in 10 million or even less [47,48]. Assuming a relatively conservative margin of 30%, a failure rate of 1.3 out of 10 million has been considered, or in other words a failure rate of $1.3 \cdot \times 10^{-7}$.

Table 4. Failure rate data of module components, given in [failures/hours].

Component	Qty. (N_j)	Value
Power switch	8	1.1×10^{-9}
Capacitor	2	2.5×10^{-9}
HF transformer	1	9.6×10^{-7}
HE Battery	28	1.3×10^{-7}
HP Battery	44	1.3×10^{-7}
HE Module		4.6×10^{-6}
HP Module		6.69×10^{-6}

Considering a unity quality factor (π_Q = 1), the reliability of one module can be calculated by using the classical exponential distribution approach of (16).

$$R_M(t) = e^{-\lambda_M t} \tag{16}$$

Since the reliability result depends on time, a period of one year has been used as a reference to carry out the subsequent calculation. In the case of HE modules which contain 28 cells in series, the module reliability result after one year is 0.96. On the other hand, HP modules contain 44 cells which give a reliability result of 0.943 after one year. By way of example and for the purpose of making a fair comparison of the results, a value of 0.95 will be set for the reliability of each of the modules. Previously, the number of series-connected modules has been defined as n_s = 8, considering one of the modules as redundant. In this situation, the fact that one of the modules is redundant means that seven are completely necessary. Without any kind of redundancy, the reliability of the system will be calculated only with seven modules, as is shown in (17).

$$R = 0.95^7 = 0.6983 \tag{17}$$

In this example, every module is necessary because if even one of them fails, the system cannot continue working. For a HESS responsible for feeding the main loads of

an electrical vessel (such as the propulsion), this is not permitted, so it will be necessary to add some redundant elements. To compute the reliability of this fault-tolerant system, a k-out-of-n structure should be developed [49].

The reliability of a k-out-of-n system with independently and identically distributed components is equal to the probability that the number of working components is greater than or equal to k (18).

$$R(k,n) = \sum_{i=k}^{n} \binom{n}{i} p^i q^{n-i} \tag{18}$$

where $\binom{n}{i}$ is the binomial coefficient which represents the number of ways to choose i elements from an n-element set. It is given by Equation (19).

$$\binom{n}{i} = \frac{n!}{i!(n-i)!} \tag{19}$$

Then, the reliability of the system can be calculated as in (20).

$$R(k,n) = \sum_{i=k}^{n} \frac{n!}{i!(n-i)!} p^i q^{n-i} \tag{20}$$

In this case, the energy storage system is composed of eight modules connected in series, where a minimum of seven modules working may be sufficient to continue operating. In this case, one of the modules can be considered as redundant (21).

$$R(7,8) = \binom{8}{7} 0.95^7 0.05 + \binom{8}{8} 0.95^8 = \underbrace{\frac{8!}{7!(8-7)!}}_{=8} 0.95^7 0.05 + \underbrace{\frac{8!}{8!(8-8)!}}_{=1} 0.95^8 = 0.9428 \tag{21}$$

As can be observed, including a redundant element considerably increases the total reliability of the system. As expected, the architecture of the energy storage unit will determine its reliability. Furthermore, it becomes even more important when a fault has already occurred, and it is operating in a partial working state.

For the sake of simplicity, some assumptions have been considered. The same 0.95 module reliability value has been taken for all cases, whether there is redundancy or not. If one of the modules fails, the performed analysis does not consider the fact that seven modules are supporting work that was previously performed by eight. This situation would probably decrease the reliability of each individual module from 0.95 to a slightly lower value since the batteries work at higher current rates. In any case, the analysis has been carried out with the aim of demonstrating the impact that adding a redundant module in series would have on the reliability of the system.

After calculating the reliability of a single branch of series-connected modules, is the time to calculate the reliability of the entire energy storage system. This system consists of nine branches connected in parallel, where five of them are HE and four are HP branches, as indicated in Table 3. Under normal conditions, all nine branches will be working. However, if one of them fails, the system could continue operating with limited power performance compared to normal operation. In any case, the case that an entire branch fails is a rather unlikely situation, since not only one but two modules on the same branch should fail for that to happen.

The series and parallel module configuration (see Figure 12) presents one module redundancy on each branch while, at the same time, it can operate with only eight of the nine branches. Taking the previously performed single branch k-out-of-n analysis as a starting point, the following step will be to compute the reliability of the nine parallel branches together. For this purpose, the reliability value calculated in Equation (21) for

a single branch will be used ($R = 0.9428$). Considering one of the branches as redundant, an eight out of nine reliability evaluation should be performed (22).

$$R(8,9) = \underbrace{\frac{9!}{8!(9-8)!}}_{=9} 0.9428^8 0.0572 + \underbrace{\frac{9!}{9!(9-9)!}}_{=1} 0.9428^9 = 0.9099 \quad (22)$$

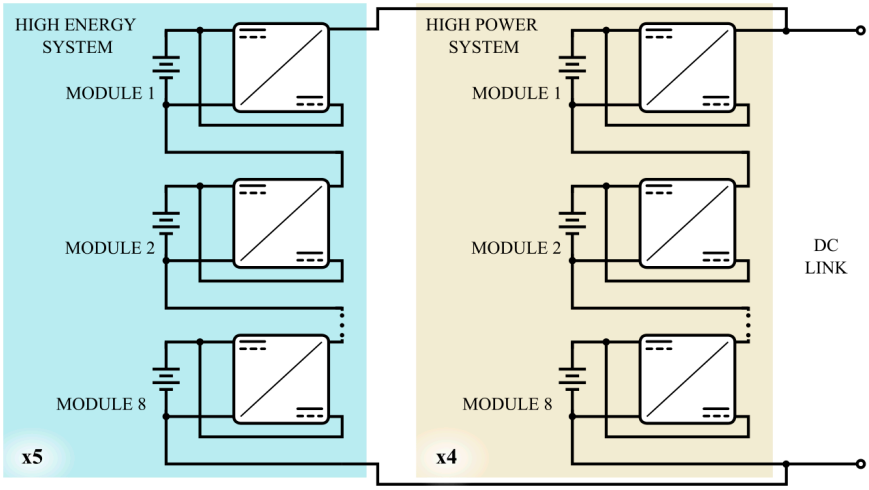

Figure 12. Simplified diagram of the hybrid storage system.

As can be seen, in this specific case, the reliability of the entire system is reduced by placing nine branches in parallel, despite the fact that one of them is redundant. The reason for this is that increasing the number of elements—in this case the number of branches—also increases the probability that one of them fails.

The same can be calculated for a different number of branches. In order to make a fair comparison, it is going to be assumed that adding the battery capacity of all the branches the result is the same. Similarly, in all cases, one of the branches will be redundant, so the system allows one of them to fail. Figure 13 shows the results of this calculation for different numbers of parallel branches. Note that these results may change if a different module reliability value is chosen at the beginning.

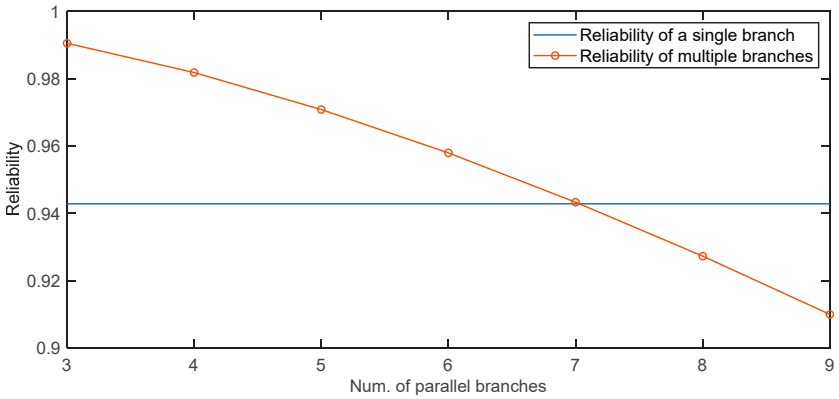

Figure 13. Reliability results from K out of n analysis for different amounts of parallel-connected branches considering 1 branch as redundant.

In conclusion, it can be stated that the introduction of redundant elements both in series and in parallel increases the reliability of the system.

A decreasing trend in reliability has also been observed as a greater number of elements is introduced: in this case, a greater number of branches in parallel. The only possible

solution to improve this would be to choose a larger cell capacity in order to connect fewer branches in parallel. This would be interesting as long as it is possible to maintain at least one redundant branch, since if the redundancy disappears, the reliability calculation would automatically be even more unfavorable.

4. Modeling and Simulation of a HESS for a Fully Electric Vessel

In the following section, a case study where a PPC for a HESS oriented to a maritime application (i.e., the electric urban ferry) is presented.

4.1. Case Study and Modeling of the Converter

4.1.1. Case Study

The selected power profile for the use case is the one presented in Figure 6. This corresponds to an urban ferry application, where two main cycles are identified.

The PPC architectures from Figure 7 require an isolated topology to avoid a short-circuit of V_{source} or V_{load}. Therefore, a dual active bridge (DAB, Figure 14) is implemented due to its simple control (phase-shift modulation, PSM), power bidirectionality and soft switching conditions. In addition, in comparison to alternative isolated topologies such as the phase-shifted full bridge, the DAB-PPC enables the implementation of lower rated voltage and current devices in the low voltage side of the converter (Q_{5-7} from Figure 14). The required phase-shift (ϕ) at each operating point is obtained from (23).

$$P_{DAB} = \frac{n \cdot V_{in} \cdot V_{out} \cdot \phi \cdot (\pi - \phi)}{2 \cdot \pi^2 \cdot f_{sw} \cdot L} \tag{23}$$

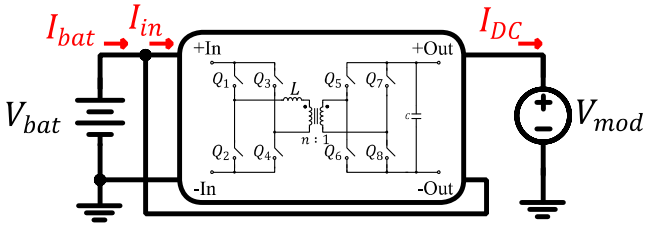

Figure 14. Simplified electrical diagram of the DAB-PPC.

Table 5 details the design parameters of each of the power converters. As it can be observed, due to the PPC configuration, a maximum voltage of 25 V is expected at the output of both converters ($V_{mod} - V_{bat}$). As a consequence, low voltage semiconductors with better conducting capabilities can be implemented. The main difference between both designs is the power level. This is defined by the power split strategy, which defines that the LTO batteries must be designed to provide higher peak power values than the NMC batteries (2.6 kW vs. 1.6 kW). Please notice that in both designs, the K_{pr} does not exceed 0.3. It must be mentioned that the simulations assume a constant battery voltage at its nominal value ($V_{bat_{NMC}}$ = 103.4 V and $V_{bat_{LTO}}$ = 101.2 V).

4.1.2. Modeling of the Converter

Regarding the modeling of the PPC, its main objective is to compute the power losses caused by the components inside the power converter. These are computed by applying (24) and (25). The energy loss at the ith time is given by E_{loss_i} and is obtained by using (24). Here, P_{loss_i} is the power loss at the ith time instant, and $P_{loss_{i-1}}$ is the power loss at the $(i-1)$th time instant. The total energy loss over the complete cycle is obtained by summing the energy loss at each time instant and is given by (25).

$$E_{loss_i} = \frac{P_{loss_i} + P_{loss_{i-1}}}{2} \cdot (t_i - t_{i-1}) \tag{24}$$

$$E_{loss_{total}} = \sum_{i=1}^{k} E_{loss_i} \quad (25)$$

where k is the total number of time instants.

Table 5. Design parameters of the DAB-PPC for the NMC and LTO strings.

Parameter	DAB-PPC (NMC)	DAB-PPC (LTO)
$P_{mod_{MAX}}$ [kW]	1.6	2.6
$P_{conv_{MAX}}$ [W]	470	770
(K_{pr})	(0.29)	(0.29)
V_{in} [V]	100	100
V_{out} [V]	25	25
n	5	5
L[µH]	63	39.6
C[µF]	300	300
f_{sw} [kHz]	50	50
Q_{1-4}	IPT111N20NFDATMA1 (V_{ds} = 200 V, R_{ds} = 11.1 mΩ)	IPT111N20NFDATMA1 (V_{ds} = 200 V, R_{ds} = 11.1 mΩ)
Q_{5-8}	IPT015N10N5ATMA1 (V_{ds} = 100 V, R_{ds} = 1.5 mΩ)	IPT015N10N5ATMA1 (V_{ds} = 100 V, R_{ds} = 1.5 mΩ)

The total P_{loss} is given by (26) and is the sum of the switching and conduction losses. The conduction loss P_{cond} is given by (27). It is obtained using the RMS of the current and the on-state resistance (R_{on}) of the devices.

$$P_{loss} = P_{cond} + P_{sw} \quad (26)$$

$$P_{cond} = R_{on} \cdot I_{RMS}^2 \quad (27)$$

The calculus of the switching losses is based on the analytical switching loss modeling described in [50,51]. Depending on the flow of the inductor current, the switching losses are classified into zero voltage switching (ZVS), incomplete ZVS (iZVS), and hard switching. In order to summarize the simulation in an image, Figure 15 presents a graphical abstract with the main steps.

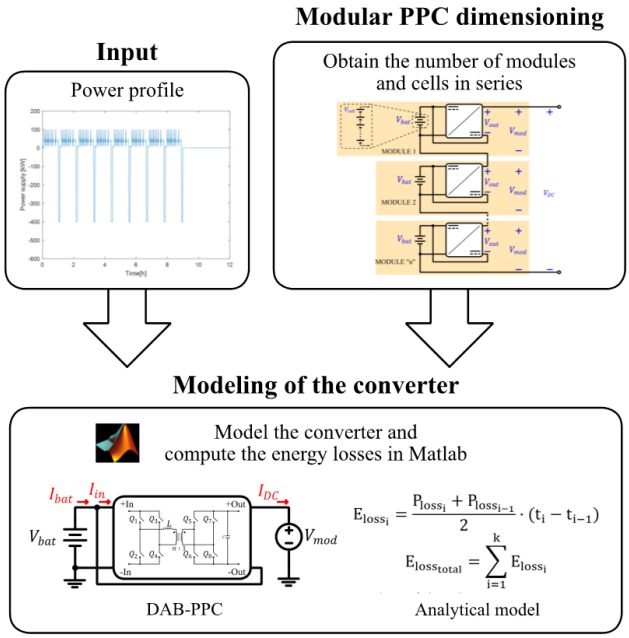

Figure 15. Graphical abstract of the numerical simulations.

4.2. Simulation Results

In the first place, Figure 16 presents the ZVS regions of each solution as a function of the voltage gain value (M) and the phase-shift (ϕ). The yellow line represents the working points of the converter through a complete charging process. As can be observed, at both solutions, this line maintains a constant M, but at different levels. This is due to the different nominal voltages for each battery technology. It can also be observed that the maximum phase-shift is designed for 45°. This way, the PSM control is designed to work inside the linear region and extra power can be delivered or absorbed by the battery whenever is necessary. Both solutions will work inside the ZVS region for a great part of the charging process except for during low power conditions. With phase-shift values close to 0, the secondary side semiconductors enter hard switching conditions. However, these semiconductors are expected to observe a reduced output voltage (Table 5).

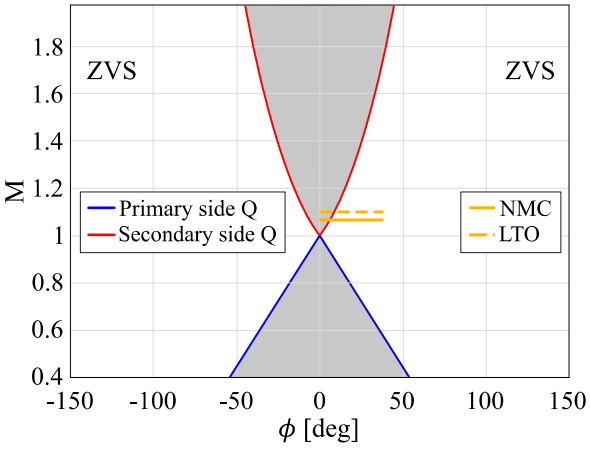

Figure 16. ZVS regions and boundaries for primary and secondary side semiconductors using PSM.

In the second place, Table 6 shows the energy losses (E_{loss}) and the total energy consumed (E_{total}) through a whole year. The energy losses are divided into conduction ($E_{conduction}$) and switching losses ($E_{switching}$). The weight of E_{loss} with respect to E_{total} is shown between parentheses. As shown in Figure 16, the secondary side semiconductors in the NMC work under hard switching conditions during a longer period than the ones in the LTO. Therefore, its switching losses have a major presence. However, since the switched voltage is very low (around 25 V, see Table 5) the switching losses are non-disturbing.

Table 6. Energy losses through one whole year.

Energy (Per Year)	NMC	LTO	Total
$E_{conduction}$ [MWh]	0.664	0.148	0.812
$E_{switching}$ [MWh]	0.220	0.075	0.295
E_{loss} [MWh]	0.884 (0.87%)	0.223 (1.99%)	1.107 (0.98%)
E_{total} [MWh]	101	11.18	112.18

5. Experimental Validation of the PPC

The converter under analysis consists of a downscaled prototype that has been designed to operate as a battery charger. The modeled charging profile of the battery is presented in Figure 17. As it can be observed, the modeled battery performs a constant current charging process by increasing its voltage and power as it is charged. Regarding the control method of the DAB-PPC, it consists of an open-loop control, in which the defined phase-shift ensures the required power consumed by the battery. For the present analysis, four test points are defined in Figure 17. "Test point 1" and "Test point 4" represent the beginning and the end of the charging process, respectively. On the other hand, "Test point 2" and "Test point 3" represent two intermediate points. Regarding V_{mod}, this parameter

represents the constant DC voltage of a single module (Figure 9). The test points defined in Figure 17 represent a battery charging process, which can be considered as a buck application ($V_{mod} > V_{bat}$). Therefore, an ISOP architecture is imposed (Figure 18a). Figure 18b,c show an image of the test bench setup. In Figure 18b, the electronic devices that form the DAB are identified, whereas in Figure 18c, each equipment used in the experimental tests is described.

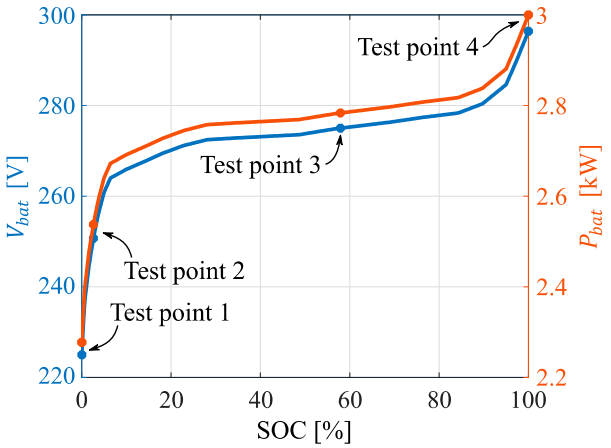

	P_{bat} [kW]	V_{mod} [V]	V_{bat} [V]
Test point 1	2.27	300	225
Test point 2	2.53	300	250
Test point 3	2.78	300	275
Test point 4	3	300	295

Figure 17. Modeled voltage and power profiles for the experimental testing of the PPC prototype.

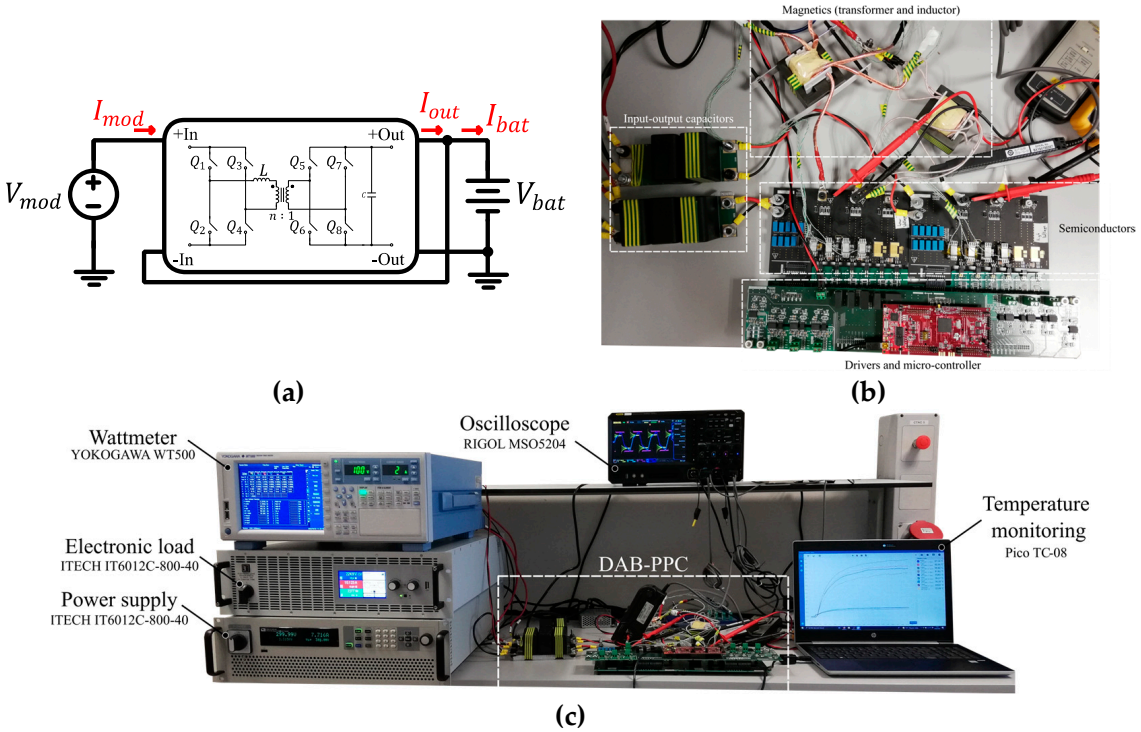

Figure 18. (**a**) Simplified electric diagram of a DAB-PPC, ISOP architecture. (**b**) DAB-PPC prototype. (**c**) System test setup.

Table 7 details the selected active and passive components. Focusing on the semiconductors, the ones from the primary side (Q_{1-4}) are designed for a maximum voltage value of 75 V ($\hat{V_{in}} = V_{DC} - \hat{V_{bat}}$). This way, reduced resistance semiconductors can be implemented. On the other hand, the secondary side semiconductors (Q_{5-8}) are designed for a maximum voltage of 295 V ($\hat{V_{out}} = \hat{V_{bat}}$). However, they are expected to observe a lower current ($I_{out} = I_{bat} - I_{DC}$).

Table 7. Active and passive components.

Components	Description
Q_{1-4}	IRFS4115-7P (V_{DS} = 150 V, R_{DS} = 11.8 mΩ)
Q_{5-8}	IPBE65R075CFD7A (V_{DS} = 650 V, R_{DS} = 75 mΩ)
n	0.2
L [μH]	15
C [μF]	200

Experimental Results

In the first place, Figure 19a presents the efficiency results obtained with the prototype at each test point. The worst case corresponds to "Test point 1", where V_{ESS} = 225 V. At this point, the battery is at its lowest value (minimum SoC) and, therefore, the voltage gain is the highest. Consequently, the power converter processes a higher amount of power. However, as the voltage increases (V_{ESS} = 250 V "Test point 2" & V_{ESS} = 275 V "Test point 3"), the power processed by the converter decreases, increasing the efficiency up to a peak value of 99.36%. In "Test point 4" (V_{ESS} = 295 V), the efficiency drops to 99.246%. This is due to an increment of the inductor RMS current. This is later explained in further detail.

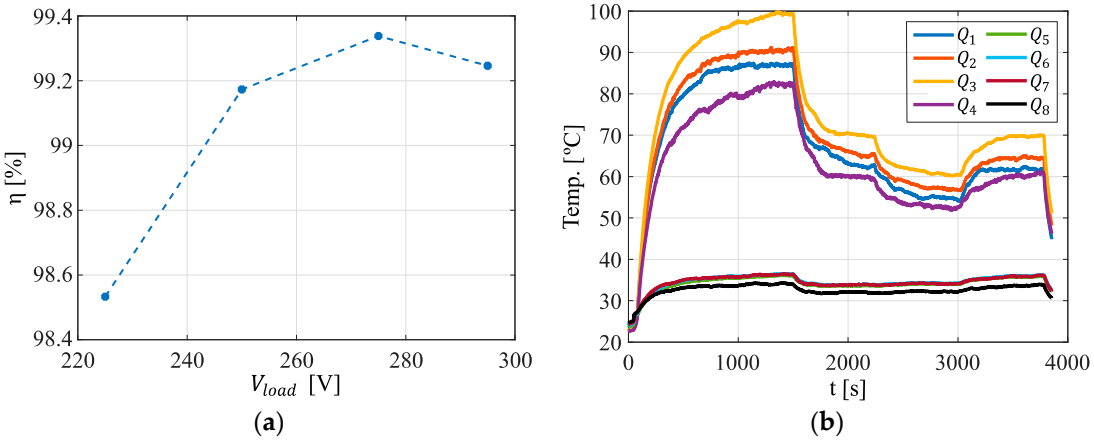

Figure 19. Experimental results. (**a**) System efficiency. (**b**) Semiconductor case temperature.

In the second place, Figure 19b presents the top-case temperature of the primary side (Q_{1-4}) and secondary side (Q_{5-6}) semiconductors. Each steady state temperature from Figure 19a represents the achieved temperature by the semiconductors in each test point. Similar to the efficiency results, the most critical working point is "Test point 1", where the hottest primary side semiconductor reach to 100 °C. When moving to "Test point 2" and "Test point 3", the temperature of the semiconductors decreases significantly, achieving a maximum value of 70 °C and 60 °C, respectively. Finally, in "Test point 4", the temperature increases again. This thermal behavior matches completely with the efficiency results from Figure 19a. The better the efficiency, the lower the temperature of the semiconductors will be. It is also very interesting to observe that the secondary side semiconductors hardly heat up at all. This is due to the reduced current that exists in the secondary side of an ISOP architecture.

Finally, related with the electrical stress suffered by the semiconductors, Figure 20 presents the steady-state waveforms of the primary and secondary AC voltages (v_{pri} and v_{sec}) and the inductor current (I_L). On the one hand, the current waveforms from Figure 20 demonstrate that the efficiency and temperature variation from Figure 19 is related to the inductor RMS current: I_{RMS_A} = 14.44 A, I_{RMS_B} = 11.61 A, I_{RMS_C} = 10.95 A, and I_{RMS_D} = 12.34 A. On the other hand, Figure 20 shows how the primary side voltage decreases from 75 V (Figure 20a) down to 5 V (Figure 20d) as the battery charges. The main benefit of this voltage reduction is that although hard switching conditions occur in

Figure 20d ($I_L > 0$ when v_{pri} is rising), they occur with only 5 V. As a consequence, the switching losses are negligible, and the semiconductors are not endangered by overvoltage.

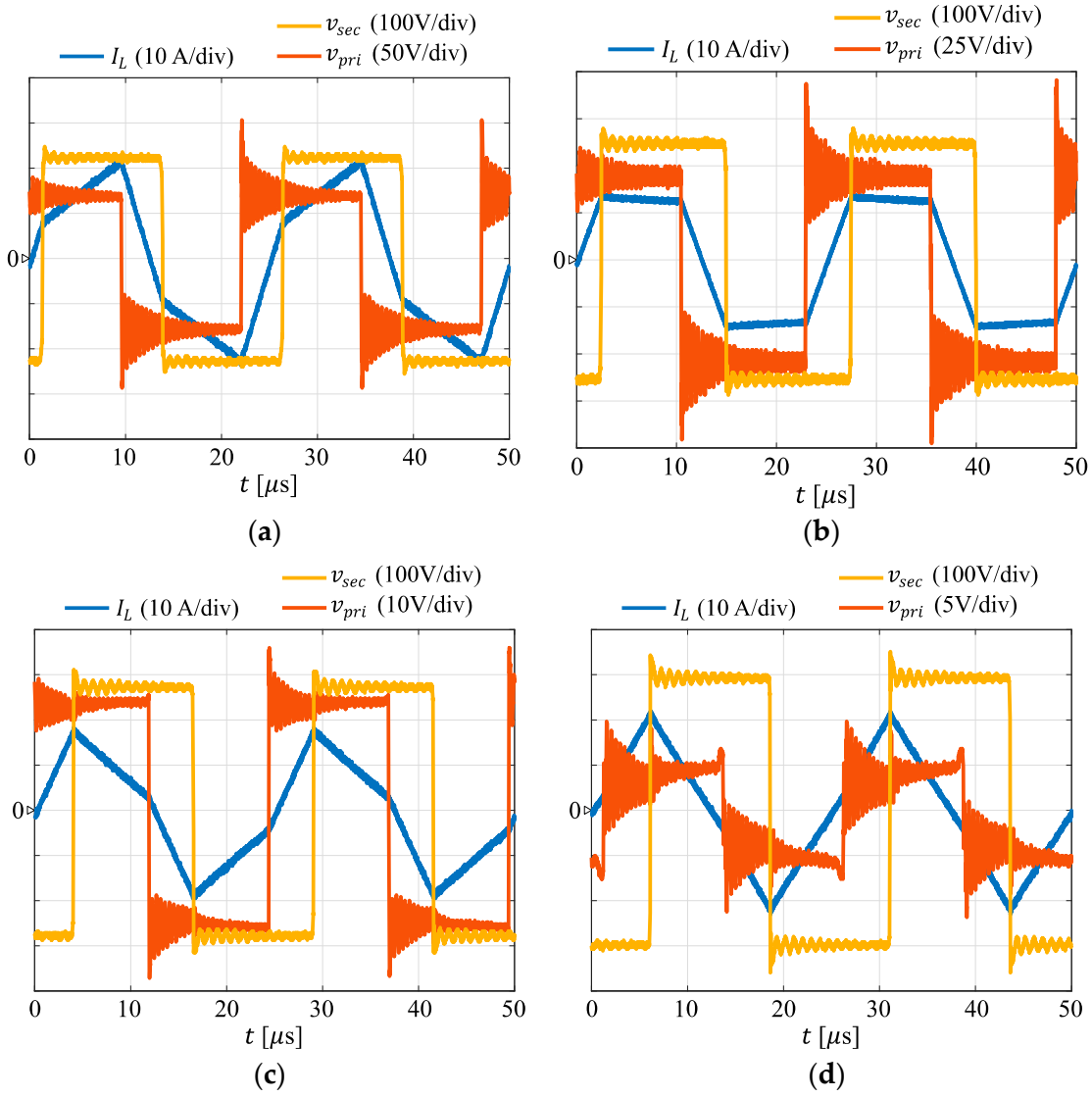

Figure 20. Steady-state experimental waveforms. (**a**) Test point 1. (**b**) Test point 2. (**c**) Test point 3. (**d**) Test point 4.

In the end, the experimental results demonstrate that the DAB-PPC is an efficient solution with low thermal and electrical stress of the devices. The peak efficiency is about 99.36%, and the temperature results show that the main hotspot is located in the primary side. Indeed, the thermal stress of the secondary side devices is almost negligible. In addition, the electrical stress of the semiconductors is reduced, as the voltage blocked by the secondary side devices decreases from 75 V to 5 V.

6. Conclusions

The electrification of the maritime sector is a promising solution to reduce GHG emissions produced by the maritime industry. An example of this is the use of ESS to power propulsion and hotel loads. Generally, single technology (monotype) batteries are used, resulting in oversized solutions that increase the cost, weight, and volume of the system. HESS can improve these aspects and, together with the appropriate converters, offer a more efficient solution.

Due to the nature of the batteries, the system output DC voltage will vary depending on the SoC of them. Therefore, it is necessary to include a converter to control the power flow and ensure a stable output voltage. In this sense, the use of smaller and more efficient power electronic converters is another key factor in the electrification of the maritime sector, where a single converter is predominantly used to process all the input power, which means higher cost and volume and compromised system reliability in the event of converter failure. In this paper, modular high efficiency converters based on PPP for fully electric vessels are presented. These converters process only a portion of the total power, reducing the converter cooling system and the total power losses. Unlike the parallel connection of PPCs, the series connection presents certain difficulties compared to full power converters. This article proposes a modular HESS solution based on the series connection of these converters to make the system flexible and scalable. In addition, as one of the challenges of using battery-based ESS is determining its optimal sizing, this work presents the sizing of a HESS for a real electric vessel that depends on the power and energy requirements of the application, the selected power split between HE and HP cells, and the cost of the cells.

Moreover, a methodology for selecting the number of modules in series together with a reliability analysis of the series and parallel connection configurations has been carried out. Although both configurations are very similar, it can be noticed that the P-S module presents higher reliability. The main conclusion that can be drawn from this analysis is that the greater the interconnection between the different elements, the greater the resulting reliability of the system.

Regarding the design of a modular PPC, a DAB is implemented due to its simple control, power bidirectionality, and soft switching conditions. With these configurations, low voltage semiconductors with better conducting capabilities can be implemented. It is observed that the series connection of the DAB-PPC presents considerable overloads if one of the series connected modules fails. However, the flow diagram for the sizing of the modular PPC presented in this paper helps to minimize the overload of the converter and the overvoltage of the switching devices. It is concluded that both can be minimized exponentially by increasing the number of modules connected in series.

A 3 kW PPC prototype was tested to demonstrate the high efficiency of this type of converters and the result were (a) as the voltage increases the power processed by the converter decreases, increasing the efficiency up to a peak value of 99.36%; (b) the thermal behavior matches completely with the efficiency results. The better the efficiency, the lower the temperature of the semiconductors will be. The secondary side semiconductors hardly heat up at all due to the reduced current that exists in the secondary side of an ISOP architecture; and (c) the primary side voltage decreases from 75 V down to 5 V as the battery charges. The main benefit of this voltage reduction is that although hard switching conditions occur, they occur with only 5 V. In consequence, the switching losses are negligible, and the semiconductors are not endangered by overvoltage.

As this article has shown, a modular HESS based on PPC can help to reduce the cost, volume, weight, and improve the flexibility of fully electric vessels. Still, there are some challenges to consider when implementing these systems. For example, one concern is that the charging infrastructure is not ready to accommodate batteries of this caliber, as they take a long time to charge, and this requires fast charging technology. Moreover, there are currently no international standards for battery installations in marine applications, although the International Electrotechnical Commission is working on standards 62619 and 62620, and classification societies have developed specific rules and/or Additional Class notation to complement some international standards. In this context, ensuring that HESS is safe and reliable is another challenge to take into account.

Finally, although the thermal and efficiency results of the DAB-PPC are very promising, potential challenges arise regarding its faulty conditions, especially due to its lack of galvanic isolation. In this sense, future research on the safety and faulty conditions of the DAB-PPC would support the implementation of PPC solutions in modular applications.

Author Contributions: Conceptualization, J.A., E.G., J.U., A.A. and R.L.-E.; software, J.A., E.G. and J.U.; validation, J.A.; formal analysis, J.A., E.G. and J.U.; writing—review and editing, J.A., E.G., J.U., A.A. and R.L.-E.; supervision, A.A. and R.L.-E.; project administration, A.A.; funding acquisition, A.A. All authors have read and agreed to the published version of the manuscript.

Funding: This research received funding from the European Union under grant agreement no. 963560 Horizon 2020 SEABAT—"Solutions for largE bAtteries for waterBorne trAnsporT". It reflects only the author's view, and the Agency is not responsible for any use that may be made of the information it contains.

Conflicts of Interest: The authors declare no conflict of interest.

References

1. Grosso, M.; Santos, F.L.M.D.; Gkoumas, K.; Stępniak, M.; Pekár, F. The role of research and innovation in europe for the decarbonisation of waterborne transport. *Sustainability* **2021**, *13*, 10447. [CrossRef]
2. Ampah, J.D.; Yusuf, A.A.; Afrane, S.; Jin, C.; Liu, H. Reviewing two decades of cleaner alternative marine fuels: Towards IMO's decarbonization of the maritime transport sector. *J. Clean. Prod.* **2021**, *320*, 128871. [CrossRef]
3. International Maritime Organization (IMO). *Fourth IMO GHG Study 2020*; IMO: London, UK, 2020.
4. Joung, T.-H.; Kang, S.-G.; Lee, J.-K.; Ahn, J. The IMO initial strategy for reducing Greenhouse Gas(GHG) emissions, and its follow-up actions towards 2050. *J. Int. Marit. Saf. Environ. Aff. Shipp.* **2020**, *4*, 1–7. [CrossRef]
5. Balsamo, F.; Capasso, C.; Lauria, D.; Veneri, O. Optimal design and energy management of hybrid storage systems for marine propulsion applications. *Appl. Energy* **2020**, *278*, 115629. [CrossRef]
6. Gagatsi, E.; Estrup, T.; Halatsis, A. Exploring the Potentials of Electrical Waterborne Transport in Europe: The E-ferry Concept. In *Transportation Research Procedia*; Elsevier B.V.: Amsterdam, The Netherlands, 2016; pp. 1571–1580. [CrossRef]
7. Wu, P.; Bucknall, R. Marine propulsion using battery power. In Proceedings of the Shipping in Changing Climates Conference, Newcastle, UK, 10–11 November 2016.
8. Alnes, O.; Eriksen, S.; Vartdal, B.-J. Battery-Powered Ships: A Class Society Perspective. *IEEE Electrif. Mag.* **2017**, *5*, 10–21. [CrossRef]
9. Mutarraf, M.U.; Terriche, Y.; Niazi, K.A.K.; Vasquez, J.C.; Guerrero, J.M. Energy storage systems for shipboard microgrids—A review. *Energies* **2018**, *11*, 3492. [CrossRef]
10. Chua, L.W.Y.; Tjahjowidodo, T.; Seet, G.G.L.; Chan, R. Implementation of optimization-based power management for all-electric hybrid vessels. *IEEE Access* **2018**, *6*, 74339–74354. [CrossRef]
11. Faddel, S.; Saad, A.A.; El Hariri, M.; Mohammed, O.A. Coordination of Hybrid Energy Storage for Ship Power Systems with Pulsed Loads. *IEEE Trans. Ind. Appl.* **2020**, *56*, 1136–1145. [CrossRef]
12. Faddel, S.; Saad, A.A.; Youssef, T.; Mohammed, O. Decentralized Control Algorithm for the Hybrid Energy Storage of Shipboard Power System. *IEEE J. Emerg. Sel. Top. Power Electron.* **2020**, *8*, 720–731. [CrossRef]
13. Thien, T.; Axelsen, H.; Merten, M.; Sauer, D.U. Energy management of stationary hybrid battery energy storage systems using the example of a real-world 5 MW hybrid battery storage project in Germany. *J. Energy Storage* **2022**, *51*, 104257. [CrossRef]
14. Naseri, F.; Barbu, C.; Sarikurt, T. Optimal sizing of hybrid high-energy/high-power battery energy storage systems to improve battery cycle life and charging power in electric vehicle applications. *J. Energy Storage* **2022**, *55*, 105768. [CrossRef]
15. Elsayed, A.T.; Mohammed, O.A. A Comparative Study on the Optimal Combination of Hybrid Energy Storage System for Ship Power Systems. In Proceedings of the IEEE Electric Ship Technologies Symposium, Alexandria, VA, USA, 21–24 June 2015.
16. Camara, M.B.; Payman, A.; Dakyo, B. Energy management based on frequency approach in an electrical hybrid boat. In Proceedings of the 2016 International Conference on Electrical Systems for Aircraft, Railway, Ship Propulsion and Road Vehicles & International Transportation Electrification Conference (ESARS-ITEC), Toulouse, France, 2–4 November 2016. [CrossRef]
17. Qin, Y.; Yang, Y.; Li, S.; Huang, Y.; Tan, S.C.; Hui, S.Y. A High-Efficiency DC/DC Converter for High-Voltage-Gain, High-Current Applications. *IEEE J. Emerg. Sel. Top. Power Electron.* **2020**, *8*, 2812–2823. [CrossRef]
18. Wang, Z.; Zheng, Z.; Li, C. A High-Step-Up Low-Ripple and High-Efficiency DC-DC Converter for Fuel-Cell Vehicles. *IEEE Trans. Power Electron.* **2022**, *37*, 3555–3569. [CrossRef]
19. Gunasekaran, D.; Peng, F.Z. Design of GaN based ultra-high efficiency, high power density resonant Dickson converter for high voltage step-down ratio. In Proceedings of the IEEE Energy Conversion Congress and Exposition (ECCE), Baltimore, MA, USA, 29 September–3 October 2019. [CrossRef]
20. Xu, L.; Guerrero, J.M.; Lashab, A.; Wei, B.; Bazmohammadi, N.; Vasquez, J.C.; Abusorrah, A. A Review of DC Shipboard Microgrids—Part I: Power Architectures, Energy Storage, and Power Converters. *IEEE Trans. Power Electron.* **2022**, *37*, 5155–5172. [CrossRef]
21. Ghimire, P.; Park, D.; Zadeh, M.K.; Thorstensen, J.; Pedersen, E. Shipboard Electric Power Conversion: System Architecture, Applications, Control, and Challenges [Technology Leaders]. *IEEE Electrif. Mag.* **2019**, *7*, 6–20. [CrossRef]
22. Hoffmann, F.; Person, J.; Andresen, M.; Liserre, M.; Freijedo, F.D.; Wijekoon, T. A multiport partial power processing converter with energy storage integration for EV stationary charging. *IEEE J. Emerg. Sel. Top. Power Electron.* **2021**, *6777*, 7950–7962. [CrossRef]

23. Anzola, J.; Artal-Sevil, J.S.; Aizpuru, I.; Arruti, A.; Lopez, R.; Alacano, A.; Bernal-Ruiz, C. Resonant Dual Active Bridge Partial Power Converter for Electric Vehicle Fast Charging Stations. In Proceedings of the 2021 IEEE Vehicle Power and Propulsion Conference (VPPC), Gijón, Spain, 25 October–14 November 2021; pp. 1–6. [CrossRef]
24. Hassanpour, N.; Blinov, A.; Chub, A.; Vinnikov, D. Soft Start and Protection of Bidirectional Buck-Boost Partial Power Converter. In Proceedings of the 3rd International Conference on Smart Grid and Renewable Energy, SGRE 2022, Doha, Qatar, 20–22 March 2022. [CrossRef]
25. Hassanpour, N.; Chub, A.; Blinov, A.; Vinnikov, D. Comparison of Full power and Partial Power Buck-Boost DC-DC Converters for Residential Battery Energy Storage Applications. In Proceedings of the 2022 IEEE 16th International Conference on Compatibility, Power Electronics, and Power Engineering (CPE-POWERENG), Birmingham, UK, 29 June–1 July 2022; pp. 5–10.
26. Anzola, J.; Aizpuru, I.; Romero, A.A.; Loiti, A.A.; Lopez-Erauskin, R.; Artal-Sevil, J.S.; Bernal, C. Review of Architectures Based on Partial Power Processing for DC-DC Applications. *IEEE Access* **2020**, *8*, 103405–103418. [CrossRef]
27. Mira, M.C.; Zhang, Z.; Jorgensen, K.L.; Andersen, M.A.E. Fractional Charging Converter with High Efficiency and Low Cost for Electrochemical Energy Storage Devices. *IEEE Trans. Ind. Appl.* **2019**, *55*, 7461–7470. [CrossRef]
28. Zientarski, J.R.R.; da Silva Martins, M.L.; Pinherio, J.R.; Hey, H.L. Evaluation of Power Processing in Series-connected Partial-power Converters. *J. Emerg. Sel. Top. Power Electron.* **2019**, *7*, 343–352. [CrossRef]
29. Iyer, V.M.; Gulur, S.; Gohil, G.; Bhattacharya, S. An Approach towards Extreme Fast Charging Station Power Delivery for Electric Vehicles with Partial Power Processing. *IEEE Trans. Ind. Electron.* **2019**, *67*, 8076–8087. [CrossRef]
30. Müller, N.; Kouro, S.; Zanchetta, P.; Wheeler, P. Bidirectional Partial Power Converter Interface for Energy Storage Systems to Provide Peak Shaving in Grid-Tied PV Plants. In Proceedings of the 2018 IEEE International Conference on Industrial Technology (ICIT), Lyon, France, 19–22 February 2018.
31. Ferreira, H.J.; Kouro, S.; Rojas, C.A.; Muller, N.; Rivera, S. Bidirectional Partial Power DC-DC Configuration for HESS interface in EV Powertrains. In Proceedings of the 2021 22nd IEEE International Conference on Industrial Technology (ICIT), Valencia, Spain, 10–12 March 2021; pp. 327–332. [CrossRef]
32. Anwar, S.; Zia, M.Y.I.; Rashid, M.; De Rubens, G.Z.; Enevoldsen, P. Towards ferry electrification in the maritime sector. *Energies* **2020**, *13*, 6506. [CrossRef]
33. Sæther, S.R.; Moe, E. A green maritime shift: Lessons from the electrification of ferries in Norway. *Energy Res. Soc. Sci.* **2021**, *81*, 102282. [CrossRef]
34. Cherchi, F.; Porru, M.; Serpi, A. Electrification of Commercial Vessels: Pilot Projects and Open Issues. In Proceedings of the 2021 IEEE Vehicle Power and Propulsion Conference (VPPC), Gijon, Spain, 25–28 October 2021; pp. 1–5. [CrossRef]
35. Kim, Y.R.; Kim, J.M.; Jung, J.J.; Kim, S.Y.; Choi, J.H.; Lee, H.G. Comprehensive design of dc shipboard power systems for pure electric propulsion ship based on battery energy storage system. *Energies* **2021**, *14*, 5264. [CrossRef]
36. Chen, R.; Yu, W.; Yang, C.F. Control strategy of an all-electric cruise ship based on cycle life mode of lithium battery pack. *Int. J. Environ. Sci. Technol.* **2022**, *19*, 8369–8384. [CrossRef]
37. Guarnieri, M.; Bovo, A.; Zatta, N.; Prandin, F.; Trovò, A. Introducing Advanced Waterborne Electric Mobility in Venice. 2022. Available online: https://ssrn.com/abstract=4175904 (accessed on 21 June 2023).
38. Degan, G.; Bucci, V.; Marino, A. A ranking method for the selection of ship energy storage systems based on batteries. In Proceedings of the 2022 International Symposium on Power Electronics, Electrical Drives, Automation and Motion (SPEEDAM), Sorrento, Italy, 22–24 June 2022; pp. 707–711.
39. Lain, M.J.; Brandon, J.; Kendrick, E. Design strategies for high power vs. High energy lithium ion cells. *Batteries* **2019**, *5*, 64. [CrossRef]
40. Miao, Y.; Hynan, P.; Von Jouanne, A.; Yokochi, A. Current li-ion battery technologies in electric vehicles and opportunities for advancements. *Energies* **2019**, *12*, 1074. [CrossRef]
41. Buchmann, I. *BU-216: Summary Table of Lithium-Based Batteries*; Battery University: Durant, OK, USA, 2021.
42. Becker, J.; Nemeth, T.; Wegmann, R.; Sauer, D.U. Dimensioning and optimization of hybrid Li-ion battery systems for EVs. *World Electr. Veh. J.* **2018**, *9*, 19. [CrossRef]
43. Zientarski, J.R.R.; Pinheiro, J.R.; Martins, M.L.D.S.; Hey, H.L. Understanding the partial power processing concept: A case-study of buck-boost dc/dc series regulator. In Proceedings of the 2015 IEEE 13th Brazilian Power Electronics Conference and 1st Southern Power Electronics Conference, COBEP/SPEC 2016, Fortaleza, Brazil, 29 November–2 December 2015. [CrossRef]
44. Zientarski, J.R.R.; Da Silva Martins, M.L.; Pinheiro, J.R.; Hey, H.L. Series-Connected Partial-Power Converters Applied to PV Systems: A Design Approach Based on Step-Up/Down Voltage Regulation Range. *IEEE Trans. Power Electron.* **2018**, *33*, 7622–7633. [CrossRef]
45. Kumar, V.; Singh, L.K.; Tripathi, A.K. Reliability Prediction Methods for Electronic Devices: A State-of-the-art Review. *IETE Tech. Rev. (Inst. Electron. Telecommun. Eng. India)* **2022**, *39*, 460–470. [CrossRef]
46. MIL-HDBK-217F(N2) Parts Count Prediction Calculator. Available online: https://reliabilityanalyticstoolkit.appspot.com/mil_hdbk_217F_parts_count (accessed on 19 June 2023).
47. Doughty, D.H.; Roth, E.P. A General Discussion of Li Ion Battery Safety. *Electrochem. Soc. Interface* **2012**, *21*, 37.
48. Roth, E.P.; Doughty, D.H. *Abuse Tolerance vs. Field Failure: Two Different Issues for Lithium-Ion Safety*; Sandia National Lab. (SNL-NM): Albuquerque, NM, USA, 2006.

49. Zuo, M.J.; Huang, J.; Kuo, W. Multi-statek-out-of-nSystems. In *Handbook of Reliability Engineering*; Springer: London, UK, 2003; pp. 3–17. [CrossRef]
50. Christen, D.; Biela, J. Analytical Switching Loss Modeling Based on Datasheet Parameters for mosfets in a Half-Bridge. *IEEE Trans. Power Electron.* **2019**, *34*, 3700–3710. [CrossRef]
51. Kasper, M.; Burkart, R.M.; Deboy, G.; Kolar, J.W. ZVS of Power MOSFETs Revisited. *IEEE Trans. Power Electron.* **2016**, *31*, 8063. [CrossRef]